Chapter 6

Ultracold Ensembles in a Strongly-Coupled Cavity

This chapter expands on the introduction of cavity QED in chapter 1 and explores the physics of many atoms coupled to a strongly-coupled cavity, including the relevant experimental regime accessed by our apparatus. Akin to the description of the atom cooling elements in chapter 2, the latter part of this chapter presents the crucial experimental systems which comprise the BEC-CQED apparatus. The definitions on the following page will be utilized throughout this chapter and the following chapter as well, where the first experiments with this system are recounted.

6.1 Introduction to Cavity Quantum Electrodynamics

As noted in the introduction, cavity QED begins with the quantization of the electromagnetic field itself. One starts with the specification of boundary conditions by which classical modes of the electromagnetic field may be defined. For example, one may take two infinite planes separated by length L, where the field must vanish at the various boundaries $\big(\mathbf{E}(x,y,0) = \mathbf{E}(x,y,L) = 0\big)$. The allowable electric field can be decomposed into the allowed eigenmodes of the "cavity"

$$\mathbf{E}(\mathbf{r},t) = \sum_j \mathcal{E}_{o,j}\phi_j(x,y)\sin(k_j z)\sin(\omega_j t - \varphi)\,\hat{\varepsilon}\,, \tag{6.1}$$

where $k_j = \pi j/L$, $\omega_j = c\pi j/L$, φ is an arbitrary phase, $\hat{\varepsilon}$ is the polarization, $\mathcal{E}_{o,j}$ is the electric field amplitude, and $\phi_j(x,y)$ is the transverse mode function. We may construct an "area" for the mode from $\iint |\phi(x,y)|^2 dxdy = A_j$, and similarly a "volume" $V_j = A_j L/2$ (the 1/2 factor is from the spatial averaging of the $\sin^2 k_j z$ function). Under field quantization [124, 32], the electric field *operator* for the same physical system is expressed as

$$\hat{\mathcal{E}}_j = \sqrt{\frac{\hbar\omega_j}{2\epsilon_o V_j}} \times \sin(k_j z) \times \left(\hat{a}_j\, e^{i\omega_j t} + \hat{a}_j^\dagger\, e^{-i\omega_j t}\right), \tag{6.2}$$

where $\hat{a}_j^\dagger$ ($\hat{a}_j$) are the creation (annihilation) operators for the j^{th} mode. The coefficient $\sqrt{\frac{\hbar\omega_j}{2\epsilon_o V_j}}$ may be regarded as the electric field per photon, and the strength of the field in the cavity is thus seen to depend on $\sqrt{1/V_j}$.

The notion of cavity QED is thus seen as the enforcement of a finite (and preferably small) mode volume V_j, resulting in a sizeable electric field per photon. For example, in this work we make use of a cavity which gives a mode volume of $V_j = 8.3 \times 10^{-14}$ m^3 for $k_j = 2\pi/(780\,\text{nm})$, yielding an electric field per photon of 416 V/m. Compared to DC fields this is not particularly large, but if this AC field interacts resonantly with an electric dipole transition in an atom or molecule, the dynamic polarizability (and thereby the AC Stark shift) may be enormous. In this work, the intensity of a single intracavity photon may exceed 50 times the saturation intensity for the D2 transition in ^{87}Rb – clearly a case where a single photon interacts strongly with a quantum system.

6.1.1 Dissipation-free Cavity QED

More precisely, we look to the Hamiltonian which governs the evolution of an atom-field system, neglecting (for the time being) the role of dissipation. We consider a two-level atom with $\hbar\omega_a$ energy difference between the excited state $|e\rangle$ and the ground state $|g\rangle$. This two-level system can be expressed with the Pauli spin operators $\hat{\sigma}^+ = |e\rangle\langle g|$ and $\hat{\sigma} = |g\rangle\langle e|$. The atom is then located in the cavity, with a single cavity mode ω_c nearly resonant with the atomic transition frequency $\omega_c \approx \omega_a$.

Ignoring the external motion of the atom, the Hamiltonian for a single atom interacting

with this cavity mode may be written as [125, 126]

$$\hat{\mathcal{H}} = \frac{1}{2}\hbar\omega_a\left(\hat{\sigma}^z + 1\right) + \hbar\omega_c\hat{a}^\dagger\hat{a} + \hbar g\left(\hat{a}^\dagger\,\hat{\sigma}^- + \hat{a}\,\hat{\sigma}^+\right), \tag{6.3}$$

where $g = \sqrt{\frac{d^2\omega_c}{2\hbar\epsilon_o V_c}}$, d is the dipole matrix element between $|e\rangle$ and $|g\rangle$, and the rotating wave approximation (RWA) has been invoked to eliminate counter-rotating terms (such as $\sigma^+\hat{a}^\dagger$). It is no understatement to say that g is *the* characteristic quantity in cavity QED. This is the Rabi frequency for an atom driven by the field from a single photon, exactly the desired coherent evolution of a system with light quanta. For the $D2$ transition in ^{87}Rb and the cavity parameters for this work (which are described later in this chapter), we obtain a theoretical maximum coupling of $g_m = 2\pi \times 15.8\,\text{MHz}$.

The lowest-order excited states of Equation (6.3) have eigenfrequencies

$$\omega_+ = \frac{\omega_a + \omega_c}{2} + \sqrt{\left(\frac{\Delta_a}{2}\right)^2 + g^2} \tag{6.4a}$$

$$\omega_a = \frac{\omega_a + \omega_c}{2} - \sqrt{\left(\frac{\Delta_a}{2}\right)^2 + g^2}\,, \tag{6.4b}$$

where $\Delta_a = \omega_c - \omega_a$. The eigenstates are superpositions of the photon excitation $|g, 1\rangle$ and atomic excitation $|e, 0\rangle$, and are deemed "cavity-like" or "atom-like" in nature given their relative amplitudes for these states. For $\Delta_a < 0$, ω_+ is atom-like and ω_- is cavity-like, the converse for $\Delta_a > 0$. On resonance, the two states are even and odd superpositions of equal amplitude.

6.1.2 Dissipation-free Cavity QED with Many Atoms

Moving beyond a single atom in a cavity, we may consider N two-level atoms in the same resonator[1]. Instead of a single two-level atom hamiltonian we require a sum over all N atoms in the system

$$\hat{\mathcal{H}}_a = \frac{\hbar\omega_a}{2}\sum_{j=1}^{N}(\hat{\sigma}_j^z + 1)\,, \tag{6.5}$$

with each atom afforded its own spatial wavefunction $\psi_j(\mathbf{r})$. It will be advantageous for basic considerations of many-atom cavity QED to assume that each atom is well localized

[1]This system was explored in the seminal paper by Tavis and Cummings [127], and the system is known as the Tavis-Cummings model.

in the axial direction to $\Delta z_j \ll 2\pi c/\omega_c$ (much smaller than the photon wavelength[2]), and similarly well-localized in the transverse direction $\Delta x_j, \Delta y_j \ll w_j$ (much smaller than the transverse mode waist). This allows us to consider ignore the features of $\psi_j(\mathbf{r})$ and assign instead a position $\mathbf{r}_j$ for the j^{th} atom. We will see that this limit is born out by all of the experimental work presented in this chapter[3].

The full Hamiltonian of the system is then

$$\hat{\mathcal{H}} = \frac{\hbar\omega_a}{2}\sum_{j=1}^{N}(\hat{\sigma}_j^z + 1) + \hbar\omega_c\hat{a}^\dagger\hat{a} + \hbar\sum_{j=1}^{N} g(\mathbf{r}_j)\left(\hat{a}^\dagger\hat{\sigma}_j^- + \hat{a}\hat{\sigma}_j^+\right). \tag{6.6}$$

It is instructive to look at the matrix representation of the lowest excitation manifold of this system, where the basis states are a single intracavity photon $|0\ldots0;\,1\rangle$ and the set of states with a single excited state atom, e.g. $|0\ldots0,1,0\ldots0;\,0\rangle$:

$$\hat{\mathcal{H}} \to \hbar\begin{pmatrix} \omega_c & g(\mathbf{r}_1) & g(\mathbf{r}_2) & g(\mathbf{r}_3) & \ldots & g(\mathbf{r}_N) \\ g(\mathbf{r}_1) & \omega_a & 0 & 0 & \ldots & 0 \\ g(\mathbf{r}_2) & 0 & \omega_a & 0 & \ddots & 0 \\ g(\mathbf{r}_3) & 0 & 0 & \omega_a & \ddots & \vdots \\ \vdots & \vdots & \ddots & \ddots & \ddots & 0 \\ g(\mathbf{r}_N) & 0 & 0 & \ldots & 0 & \omega_a \end{pmatrix}. \tag{6.7}$$

This $N \times N$ Hamiltonian of course has N eigenstates, but only two of these are excited by cavity transmission[4] [129]. The eigenfrequencies of system are

$$\omega_+ = \frac{\omega_a + \omega_c}{2} + \sqrt{\left(\frac{\Delta_a}{2}\right)^2 + \sum_{j=1}^{N}|g(\mathbf{r}_j)|^2} \tag{6.8a}$$

$$\omega_- = \frac{\omega_a + \omega_c}{2} - \sqrt{\left(\frac{\Delta_a}{2}\right)^2 + \sum_{j=1}^{N}|g(\mathbf{r}_j)|^2}, \tag{6.8b}$$

where again we distinguish "cavity-like" excitations and "atom-like" excitations. Before proceeding, it is important to note that the eigenstates associated with these energy states

[2]This is also known the *Lamb-Dicke* regime.

[3]Though many interesting future experiments could be imagined where the atomic wavefunctions are delocalized over a larger spatial range [128].

[4]The remaining $N-2$ excited states are all degenerate at energy $\frac{\hbar\omega_a}{2}$, and are not excited by cavity transmission because they have zero amplitude for an intracavity photon. The presence of these states does guarantee that, when conducting the absorption imaging on the *side* of cavity as discussed in chapter 7, the atomic resonances will not be shifted.

of this Hamiltonian obey a symmetry on the atomic excitations. The action of $\sum_{j=1}^{N} \hat{\sigma}_j^+$ on the atomic ground state $|\tilde{0}\rangle = |0 \ldots 0\rangle$ results in an (unnormalized) excited state

$$\sum_{j=1}^{N} \hat{\sigma}_j^+ |0 \ldots 0\rangle = \sum_{j=1}^{N} |\delta_{1j}, \delta_{2j}, \ldots \delta_{Nj}\rangle \,, \tag{6.9}$$

where δ_{ij} is the Kronecker delta. Such excitations were elucidated by Dicke [116] as cooperative spin states, where the symmetry represents the fact that generally it will not be "known" which atom from the ensemble is excited. The first atomic excitation is thus defined

$$|\tilde{1}\rangle = \frac{1}{\sqrt{N}} \sum_{j=1}^{N} |\delta_{1j}, \delta_{2j}, \ldots \delta_{Nj}\rangle \,. \tag{6.10}$$

or, using Dicke's original "cooperation number" formalism, $|\tilde{0}\rangle = |\frac{N}{2}, -\frac{N}{2}\rangle$ and $|\tilde{1}\rangle = |\frac{N}{2}, -\frac{N}{2}+1\rangle$. This symmetric excitation has many important consequences, highlighted by the large body of work with such collective effects in atomic ensembles [130, 131, 132, 133, 134], and one need look no further than the previous chapter's discussion of superradiance to see yet another example of the importance of these collective excitations.

In Equation (6.6) we do not immediately obtain these perfectly symmetric Dicke states, as the analogous collective raising operator is rather $\sum_{j=1}^{N} g(\mathbf{r}_j)\hat{\sigma}_j^+$. Thus, the modified first atomic excited state is

$$|\tilde{1}'\rangle = \left(\frac{1}{\sum_{j=1}^{N} |g(\mathbf{r}_j)|^2} \right) \sum_{j=1}^{N} g(\mathbf{r}_j) |\delta_{1j}, \delta_{2j}, \ldots \delta_{Nj}\rangle \,, \tag{6.11}$$

where the state $|\tilde{1}\rangle$ enters only under identical coupling for all atoms. We need not invoke this limit, as it is unlikely to be the case experimentally and the energy level structure can be understood regardless. The important point is to consider excitations of the system which treat all atoms of the system symmetrically, weighted by $g(\mathbf{r})$.

It will be convenient to define g_{eff}, the effective cavity coupling per atom, as $g_{eff}^2 = \frac{1}{N}\sum_{j=1}^{N} |g(\mathbf{r}_j)|^2$. The eigenvalues in Equation (6.8) thus simplify to

$$\omega_+ = \frac{\omega_a + \omega_c}{2} + \sqrt{\left(\frac{\Delta_a}{2}\right)^2 + N g_{eff}^2} \tag{6.12a}$$

$$\omega_- = \frac{\omega_a + \omega_c}{2} - \sqrt{\left(\frac{\Delta_a}{2}\right)^2 + N g_{eff}^2} \,, \tag{6.12b}$$

Generally we may regard value of g_{eff} as dependent on "internal" and "external" factors. External factors include the spatial positions of atoms in the mode and the atomic wavefunctions (if they are relevant). As will be the case for this work, an evenly distributed of ensembles of atoms in the Lamb-Dicke limit amidst the $\sin k_p z$ standing wave mode will yield an external factor of $\frac{1}{2}$.

The internal factors include the elements which contribute to the dipole moment, e.g. the Clebsch-Gordon coefficients for a transition driven with by polarized light. Again considering an example relevant for this work, we look to driving a collection of $|F = 1, m_F = -1\rangle$ ^{87}Rb atoms on the $D2$ transition. By convention, the cavity coupling is expressed as the maximum coupling for the $\langle J|e\mathbf{r}|J'\rangle$ dipole transition, and then the hyperfine matrix elements for the transitions are given by the Clebsch-Gordon coefficients for the transitions [135]. We may consider probing the these atoms with either σ^+, π, or σ^- light. The respective squared coefficients for $D2$ transitions from this manifold are summarized in the inset of Figure 6.1.

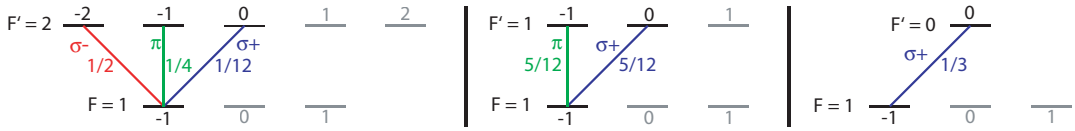

Figure 6.1: (a) Relevant Clebsch-Gordon spectrum for $D2$ transitions of $|F = 1, m_F = -1\rangle$ atoms. Squared values connect σ^- (red), π (green), and σ^+ (blue) transitions to the $F' = 2, 1, 0$ excited state manifolds.

As will be the case in the far-detuned limit described in the subsequent section, the atom-cavity detuning Δ_a can be large enough to render the excited-state hyperfine energy splitting negligible. In this case, the direct quadrature sum of the Clebsch-Gordon coefficients for the appropriate transition gives the modified g^2 coupling. For example, for the maximum coupling for a σ^+ polarized probe on the $D2$ transition from the

$|F = 1, m_F = -1\rangle$ is given by

$$\begin{aligned} g_o^2 &= g_m^2 \sum_{k=-1}^{+1} |c_{1,-1;1+k,-1+k}|^2 \\ &= g_m^2 \left(\frac{1}{12} + \frac{5}{12} + \frac{1}{3} \right) \\ &= \frac{5}{6} g_m^2 \,. \end{aligned} \tag{6.13}$$

This represents the maximum *attainable* coupling from the $|F = 1, m_F = -1\rangle$ state. With a few notable exceptions outlined in the chapter 7, this is taken as the new cavity coupling standard for the system, with $g_o = 2\pi \times 14.4\,\mathrm{MHz}$. Thus, the effective cavity coupling is given by

$$\begin{aligned} g_{eff}^2 &= (external) \times (internal) \times g_m^2 \\ &= \frac{1}{2} g_o^2 \,, \end{aligned} \tag{6.14}$$

the value of which was memorized at $g_{eff}^2 = (2\pi)^2 \times 104\,\mathrm{MHz}^2$ because of its ubiquity in practice.

6.1.3 The Far-Detuned Limit ($\sqrt{N} g_o \ll |\Delta_a|$)

The "resonant regime," where $|\Delta_a| < g_o$ has been explored by a number of experimental groups [37, 43, 136]. In this limit, the eigenenergies in Equation (6.12) become simply $\omega_\pm = \omega \pm \sqrt{N} g_{eff}$. For small atom number, this may also be regarded as the "absorptive" regime because the excitation probability per atom can be sizeable. In a particularly nice experiment, McKeever *et al.* [137] measured directly one, two, three, and four cesium atoms in a strongly coupled cavity by the $\sqrt{N}$ dependence of the eigenfrequencies.

For the work presented in this document, we consider instead the "far detuned limit," where $\sqrt{N} g_o \ll |\Delta_a|$ (Figure 6.2). Here, the excitations are *decidedly* cavity-like and atom-like in character, as shown. The eigenvalues take on a very different character from the resonant regime:

$$\widetilde{\omega}_c = \omega_c + \Delta_N \tag{6.15a}$$

$$\widetilde{\omega}_a = \omega_a - \Delta_N \,, \tag{6.15b}$$

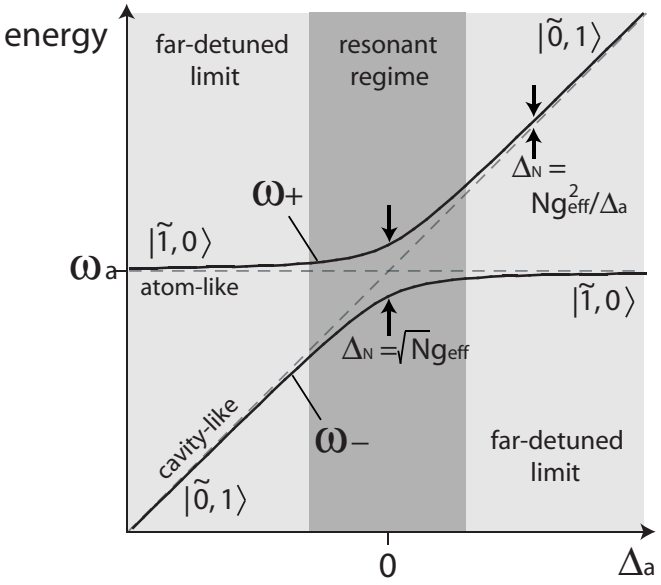

Figure 6.2: Energy level avoided crossing in the many-atom cavity system, highlighting the distinction between the resonant regime and the far-detuned limit.

where $\Delta_N \equiv \frac{Ng_{eff}^2}{\Delta_a}$. This shift is linear with the atom number, and the "per-atom" shift is given by g_{eff}^2/Δ_a, simply the far-detuned AC Stark shift associated with atoms interacting with the single cavity photon. The sketch of the level structure for $|\Delta_a| \gg \sqrt{N}\, g_o$ with $\Delta_a > 0$ is shown in Figure 6.3.

As depicted in the Figure, this system will be probed by laser light which is detuned from the bare cavity resonance by $\Delta_c = \omega_p - \omega_c$. The system will be in resonance when $\Delta_c = \Delta_N$, resulting in full transmission of the probe. In driving the cavity off resonance $\Delta_c \neq \Delta_N$, the transmission is suppressed and the probe light will reflect off the cavity. While the level structure depicted in Figure 6.3 is indisputably simple, as in the case of single atom CQED even simple level structures can bring surprises. Life gets interesting when both the dissipation mechanisms and the role of the probe field are considered, which respectively are the subjects of the following two sections.

It should be noted that while we have only considered the first manifold in the Tavis-Cummings model [127], this is as far as we need to go even in the case of many photon excitations in the cavity. If $\bar{n} \ll N$, as will be the case in this work, the excitation proba-

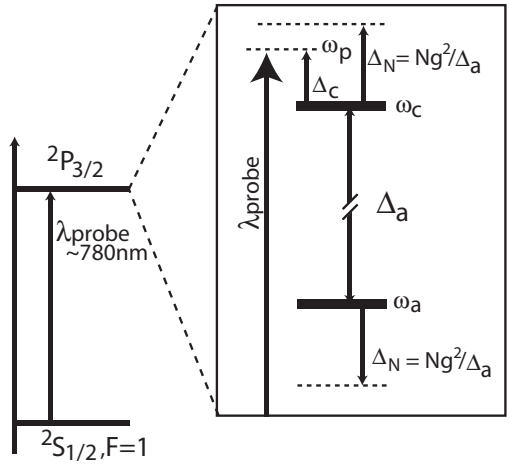

Figure 6.3: Dispersive energy level structure. This is a "blue" cavity, in that the cavity resonance is of higher frequency than the atomic transition. The cavity shift Δ_N is thereby also positive, shifting the atom-cavity resonance.

bility per atom is always small and the higher manifolds are irrelevant [129]. The largest intracavity photon number was $\bar{n} \sim 20$, compared to typical atom numbers measured in the 10's of thousands.

6.2 Dissipation

The crucial role of dissipation in a realistic cavity QED system has been ignored thus far, and to proceed we must now account for the system losses. The process of spontaneous emission is familiar, taking the atomic excitation $|\tilde{1}', 0\rangle \rightarrow |\tilde{0}, 0\rangle$ at a rate γ. For the $D2$ transition in ^{87}Rb, the atomic field decay rate is $\gamma = 2\pi \times 2.99\,\mathrm{MHz}$ [135]. As for the cavity decay, if the mirrors are realistic reflectors with combined transmission and scattering losses of rate κ, the amplitude of the excited state $|\tilde{0}, 1\rangle$ will decay as $\exp(-\kappa t)$ to the ground state $|0, \tilde{0}\rangle$. As κ is the half-linewidth of the cavity, it also sets the cavity transmission. For a monochromatic probe, the transfer function of the (empty) cavity is $(1 + \Delta_c^2/\kappa^2)^{-1}$.

Detailed models involving master equations for a driven atom-cavity system in the presence of dissipation may be found elsewhere [138], but the coherent evolution rate

g_o should be surely be stacked up against the decay rates κ and γ.[5] This leads to the identification of some dimensionless quantities which characterize cavity QED systems. The single atom cooperativity $C_1 = g_o^2/2\kappa\gamma$ can be thought of as the square of a Q-factor, where in this case the "oscillator" is the coherent oscillation of energy between the atom and the cavity photon at frequency $2g_o$. The critical atom number is defined as $n_a = 2\kappa\gamma/g_o^2 = 1/C_1$, which quantifies the number of intracavity atoms required to significantly alter the optical response of the system. The critical photon number is $n_p = \gamma^2/2g_o^2$, which quantifies the number of intracavity photons which saturate the atomic system. The regime of "strongly-coupled" cavity QED can be identified as the situation where $(n_a,\, n_p) \ll 1$, i.e. a high-Q oscillator with single atoms and single photons.

We now move past the basic theoretical considerations of many-atom cavity QED and on to the practical considerations in implementing such a system.

6.3 The BEC-CQED System

In this section, we describe the integrated elements of the full system BEC-CQED apparatus as it functions in this capacity. The subsystems can roughly be compartmentalized into the cavity system itself, the cavity stabilization system, the cold atom delivery, and the finally the probing/detection system.

6.3.1 The Cavity

The cavity decay rate κ is related to the separation and reflection/transmission properties of the mirrors. Following Hood *et al.*, each mirror is characterized by intrinsic transmission $\mathcal{T}$ and loss $\mathcal{L}$ coefficients, which relate the cavity finesse $\mathcal{F}$ as

$$\mathcal{F} = \frac{2\pi}{all\,losses} = \frac{\pi}{\mathcal{T} + \mathcal{L}}\,. \tag{6.16}$$

For the REO mirrors used in this work, Deep Gupta measured $\mathcal{T} = 1.6\,\text{ppm}$ and $\mathcal{L} = 3.8\,\text{ppm}$, translating to an expected finesse of $\mathcal{F} = 580,000$. At room temperature, the cavity itself has a length of $192.3\,\mu\text{m}$. During experimental operation, the cavity length *lengthens* to $194\,\mu\text{m}$ from the radiative thermal coupling between the cavity mount and

[5] They are normally expressed together as (g_o, γ, κ), with values of $2\pi \times (14.4, 2.99, 0.66)$ for our system.

k_p	: Cavity probe wavevector	$2\pi/780\,\text{nm}$
L_{RT}	: Cavity length (lN_2 off)	$192.3\,\mu\text{m}$
L	: Cavity length (lN_2 on)	$194\,\mu\text{m}$
R	: Radius of curvature	$5\,\text{cm}$
w_p	: TEM_{00} mode waist for 780 nm	$23.4\,\mu\text{m}$
V_m	: Mode volume $\left(\pi w_p^2 L/4\right)$	$8.27\times10^4\,\mu\text{m}^3$
ν_{fsr}	: Free spectral range	$780\,\text{GHz}$
$\mathcal{T}$	: Mirror transmission @ 780 nm	$1.6\,\text{ppm}$
$\mathcal{L}$	: Total mirror losses @ 780 nm	$3.8\,\text{ppm}$
$\mathcal{F}$	: Cavity finesse @ 780 nm	584,000
$\mathcal{F}_t$	: Cavity finesse @ 850 nm	38,000 (avg)
g_o	: Maximum cavity coupling	$2\pi\times14.0\,\text{MHz}$
κ	: Cavity loss rate	$2\pi\times0.66\,\text{MHz}$
γ	: Spontaneous emission rate	$2\pi\times2.99\,\text{MHz}$
n_a	: Critical atom number $(1/C_1)$	0.019
n_p	: Critical photon number $(\gamma^2/2g_o^2)$	0.018
C_1	: Single-atom cooperativity $(g_o^2/2\kappa\gamma)$	51.4
C	: Collective atomic cooperativity $(Ng_{eff}^2/2\kappa\gamma)$	$\lesssim 2.5\times10^6$

Table 6.1: Cavity QED Parameters

the liquid-nitrogen cooled millitrap mount[6]. During these experimental conditions,the free spectral range is $\nu_{fsr} = 780\,\text{GHz}$ ($\Delta\lambda_{fsr} = 1.5\,\text{nm}$). The full cavity linewidth 2κ may be measured by a simple cavity ringdown measurement which measures the $1/e$ decay time of light transmission as the cavity is swept rapidly across resonance (i.e. $\frac{d}{dt}\Delta_c \gg \kappa^2$). Repeated ringdown measurements have consistently shown a $1/e$ time of $\sim 120\,\text{ns}$, implying $\kappa = 2\pi\times0.66\,\text{MHz}$. As the usual definition of the finesse [139] is the ratio of the free spectral range to the full cavity linewidth. As κ is the *half*-linewidth, we have $\mathcal{F} = \pi\nu_{fsr}/\kappa = 5.9\times10^5$, right in line with the theoretical value. The topic of probing and detection will be revisited later in this chapter, but it is important to note that while the intracavity photons are lost at a rate 2κ they are not necessarily emitted towards the detector (presumably placed on one side of the cavity). For a cavity with identical mirrors, the probability that an intracavity photon decay will result in a detectable photon is $\mathcal{T}/2(\mathcal{T}+\mathcal{L}) = 0.15$.

[6]That the cavity length increases seems counterintuitive, but between the small thermal mass and the fact that the glass cavity structure "sees" almost no solid angle that is *not* the cold millitrap surface $\sim 0.25\,\text{mm}$ away, it is no surprise that the cavity mirrors cool to a temperature lower than their bulk copper support structure (described later). The cavity length did fluctuate some during data runs, leading to many annoying stoppages as the cavity length wandered beyond the dynamic range of the tuning PZT, requiring re-locking at the next free spectral range.

Table 6.1 summarizes the relevant cavity QED parameters for our system. We may compare our system to some other notable many-atom CQED implementations, which typically look to the *many-atom* cooperativity as an important figure of merit for ensemble-based protocols for [140, 141, 142, 131]. It is strictly defined as [138]

$$\begin{aligned} C &\equiv \frac{1}{2\kappa\gamma}\sum_{j=1}^{N}|g(\mathbf{r}_j)|^2 \\ &= N\frac{g_{eff}^2}{2\kappa\gamma} = NC_1\,. \end{aligned} \tag{6.17}$$

For the system described in chapter 7, we were able to place up to $N = 10^5$ atoms inside the cavity described in this section, and with the $\frac{1}{2}$ spatial averaging factor this gives a collective atomic cooperativity of $C = Ng_o^2/4\kappa\gamma = 2.5 \times 10^6$. Comparing this with two recent experiments by Sauer *et al.* ($C = 5.4 \times 10^3$, in a strongly-coupled system [49]) and Tuchman *et al.* ($C = 1.2 \times 10^4$, in a weakly-coupled system [56]), we have achieved the largest collective cooperativity ever reported, two orders of magnitude over the previous state of the art.

Lost perhaps, in the usual discussion of optical properties and cavity QED parameters, is the sizeable mechanical infrastructure upon which such a cavity rests. That our cavity must integrate with the two chapters worth of architecture already described makes the cavity infrastructure worth a close look.

6.3.2 The Cavity Mount

A small but very important element of the cavity system is the "payload" piece which rests at the end of the second mass and holds the cavity. This mount is actually two pieces designed to mate the cavity with the millitrap. To accomplish this, the mirror faces must be spatially separated so that they may bridge the faceplates (see chapter 3), and then returned to their original 192.3 μm separation. Figure 6.4 shows the pieces upon which the cavity mirrors rest. The threaded bolt allows the two interlocking copper pieces to be spread apart while remaining a single unit. During installation into the main chamber, the mirror faces are spread apart by ~ 1 cm. The cavity is then positioned into the central channel of the millitrap center piece. After the cavity mirrors are in their proper $x - y$

positions, the pieces are contracted so that the cavity mirrors have threaded the faceplate apertures. The goal was that the cavity mirrors never touch the millitrap in spite of the very narrow clearances, although during installation and a handful of times since[7] this occurred without any detrimental effects. When this happens, the 3D translation stage (described in the next section) is just used to walk the cavity back into place.

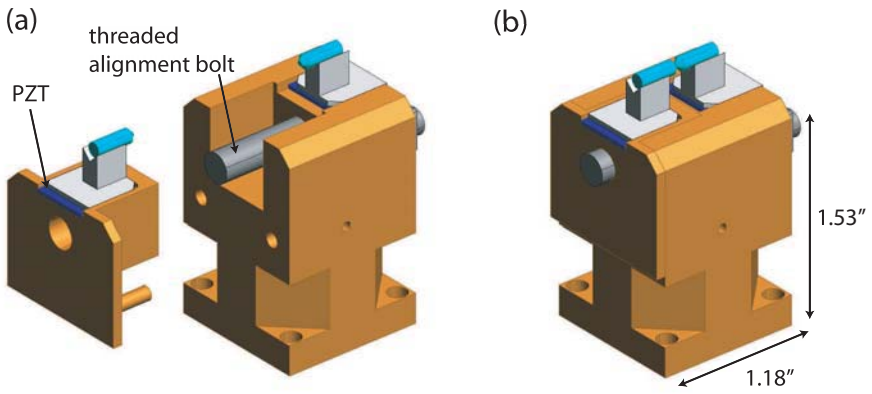

Figure 6.4: The retractable cavity mount. (a) The two cavity mount pieces (a) separated and (b) mated. The threaded alignment bolt ($1/4 - 20$ stainless steel hex cap) allows the linear travel which separates the cavity mirrors for both integration with the millitrap (its essential function) and cleaning (its very handy incidental function).

6.3.3 Cavity Stabilization

Implicit in the theoretical treatment of the cavity resonance is that the cavity has well-defined resonances. To accomplish this, the cavity must be "locked" to a specific frequency, meaning that the mirror separation L must be set to high precision. The system requirements are substantial, as one considers what level of length stabilization is required. The cavity frequency must be stabilized much tighter than its linewidth 2κ, and the cavity resonance itself is probed at roughly $\lambda_p = 780\,\text{nm}$, or $\omega_p = 2\pi \times 3.8 \times 10^{15}\,\text{Hz}$. This is ≈ 490 times the free spectral range $\nu_{fsr} = \frac{c}{2L} = 7.8 \times 10^{11}\,\text{Hz}$. From this, the

[7] The 4.2 magnitude earthquake on March 1st, 2007 which crashed the cavity was a notable instance.

length change ΔL which will shift the cavity by a single linewidth may be shown to be

$$\begin{aligned} \Delta L &\approx \frac{\lambda\kappa}{4\pi\nu_{fsr}} \\ &\approx \frac{\lambda}{2\mathcal{F}} \\ &\approx 0.7\text{pm}\,, \end{aligned} \tag{6.18}$$

where the finesse enters from $\mathcal{F} = \kappa/2\pi\nu_{fsr}$. Within its bandwidth the lock must stabilize the cavity length to much less than this level, putting the required length accuracy into the 10^{-13} m range. This is an incredibly small length, but the sensitivity of the cavity itself makes this possible.

The cavity stabilization takes two forms, a passive vibration isolation system and an active locking component. The passive system is designed to eliminate high frequency > 10 kHz mechanical vibrations, and follows similar systems used in scanning tunneling microscopes (STMs) [143]. The principle is merely one of spring-mass filtering, where the sensitive element (the cavity) is coupled to the environment (the chamber/laboratory) through interspersed "springs" and masses. Generally, large masses and springs of low spring constant K are desirable, although the very low-K springs used in modern STM systems were inappropriate because they would allow the cavity a range of motion which could crash the mirrors into the millitrap. We utilized instead Viton®, a UHV compatible rubber, as the intermediary "spring" element upon which the cavity mount pieces rest. The mounting masses were 0.5 kg and 2.9 kg, and their shape was designed to simultaneously rest on the 3D translation stage (Thermionics EC-1.39-2, which controls the positioning of the cavity), and fit into the main UHV chamber to mate with the millitrap. The full vibration isolation system is shown in Figure D, and the design drawings are presented in Appendix D.

Initial design estimates for the two mechanical resonant frequencies were $f_1 \approx 200$ Hz and $f_2 \approx 1000$ Hz, commensurate with Deep Gupta's measurements of the cavity resonances to be $f_1 \lesssim 70$ Hz and $f_2 \sim 800$ Hz. After the second resonance, the displacement transfer function falls off as $1/f^4$, strongly suppressing the high frequencies which would plague the cavity system.

To eliminate the low-frequency vibrations, piezo-electric transducers (PZTs) are em-

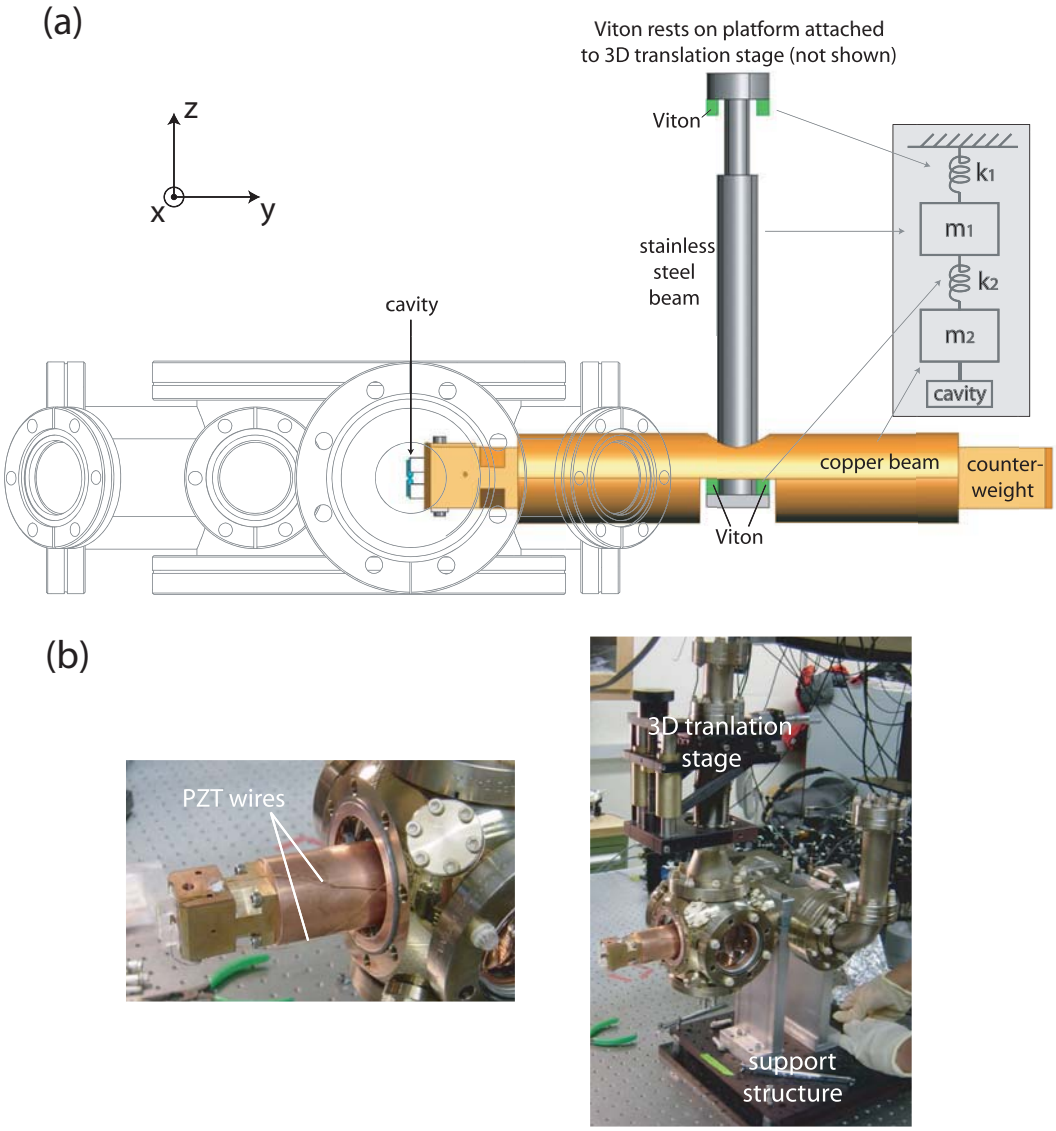

Figure 6.5: The cavity mounting structure. (a) The passive vibration isolation system is seen in context. The T-shaped structure is designed to mate with the main chamber, yet allow 3D positioning of the entire mounting system. The steel beam rests on a platform attached to a 3D translation stage which allows fine adjustments of the entire assembly. The Viton® pieces serve as the "springs" and the steel/copper beams are the "masses" in an idealized coupled oscillator system, diagrammed on the inset. The cavity payload is seen in its final position inside the main chamber. (b) The photos show the cavity prior to installation in the chamber, with critical elements labeled.

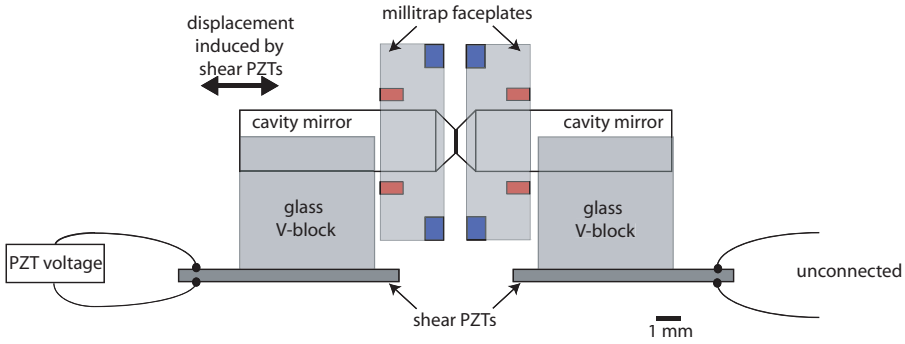

Figure 6.6: The cavity-PZT system. Shown are the elements of the cavity mounting platform, including the shear PZTs which control the cavity length. Both mirrors rest on PZT elements, a redundancy which both ensures identical height off the platforms/cavities and provides a backup in case the wired PZT element was to malfunction.

ployed to actively stabilize the cavity length. The cavity mirrors rest on glass[8] V-blocks, which are in turn epoxied to the PZT elements. This assembly is depicted in Figure 6.6. The maximum voltage on the PZTs is $\sim 500\,\mathrm{V}$, and the voltage was kept to $< 450\,\mathrm{V}$. This limited the range of the cavity PZT tuning to just greater than one free spectral range. The bandwidth of this active locking was limited by these PZTs, as the feedback had to be cutoff at $\lesssim 1\,\mathrm{kHz}$ to avoid uncontrolled resonances in the ceramic material.

Stabilizing the cavity requires no less than three independent servo controls, as shown in Figure 6.7. The "length standard" in the system was the *transfer cavity*, which is a Fabry-Perot cavity of length 30 cm, $\nu_{fsr} = 500\,\mathrm{MHz}$. The transfer cavity mirrors had radius of curvature 25 cm, and half-linewidths of $\approx 100\,\mathrm{kHz}$ at 850 nm, $\approx 30\,\mathrm{kHz}$ at 780 nm (CVI Laser TLM2-800-0-0537-0.25CC). The transfer cavity rests on Sorbothane® squares inside a stainless steel cylinder, which also rests on Sorbothane® to eliminate vibrations. The cylinder is evacuated to prevent air currents from disturbing the locks.

In practice, the sequence of locking was as follows. The 780 nm probe laser is tuned to the desired atomic detuning Δ_a. The ECDL was then frequency stabilized to the transfer cavity via Pound-Drever-Hall (PDH) locking (on transmission) after $\sim 300\,\mathrm{kHz}$ sidebands

[8]These pieces (custom manufactured by Mindrum Precision) are constructed out of glass so that they have the same coefficient of thermal expansion as the mirrors themselves, thereby reducing stresses which could cause modification of the optical properties (i.e. birefringence) of the mirrors.

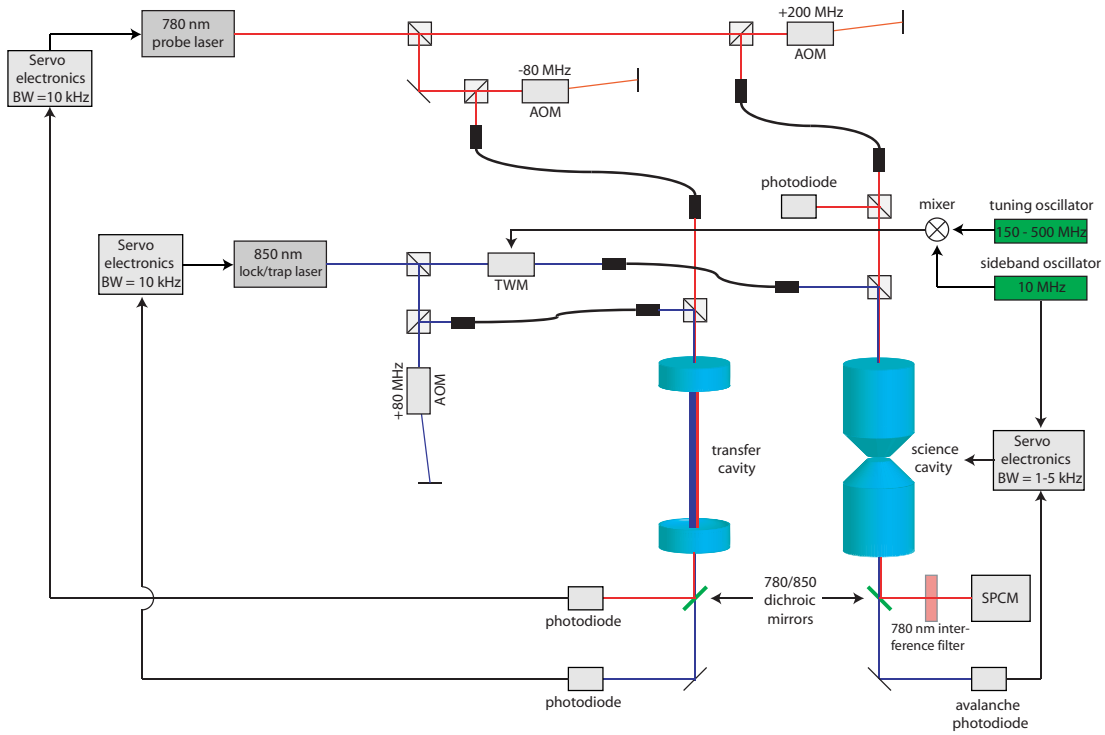

Figure 6.7: The cavity laser feedback system. The locking procedure is outlined in the text, but of special note on this diagram is special role of the two modulation frequencies on the 850 nm locking light. The $150-500$ MHz tuning oscillator allows the locked cavity to be fine-tuned by the variation of the sideband frequency, which is the "carrier" for the cavity lock. The 10 MHz secondary sidebands are the "modulation" sidebands which are mixed down to provide the PDH locking signal for the cavity.

were induced with a double-pass acousto-optic modulator. Turning to the science cavity, both the 780 nm probe and 850 nm locking light are impinged on the cavity, which is in "sweep" mode at this stage to locate the frequencies of the two lasers. The probe laser is then monitored on reflection off the cavity, and the 850 nm locking laser was monitored on transmission by an avalanche photodiode (APD). The 850 nm light was modulated with a traveling wave electro-optic modulator (TWM) with a mixed signal including the primary "tuning" sideband (of range $150-500$ MHz) and the secondary "locking" sideband ($\sim$ 10 MHz). The 850 nm laser is then tuned such that one of the primary sidebands overlaps with the stationary 780 nm probe. The 850 nm laser is then locked to the nearest lockable transverse mode of the transfer cavity. Fine tuning of the primary sidebands

overlapped the 850 nm and 780 nm beams on the science cavity, which is finally locked by PDH on transmission to the APD with the secondary 10 MHz sidebands.

It is important to note here that, while locked, the cavity *always* has some level of 850 nm locking light inside. The probe can be engaged/extinguished at will, but we found that the locking light cannot drop below 100 nW at the APD without losing the cavity lock. The AC Stark shift of this red-detuned light is irrelevant, but higher intracavity powers can be significant enough to confine the atoms in the standing wave potential of the locking light. This feature of a controlled optical trap functionality is a hallmark of the subsequent chapter. Thus, the phrase "locking light" and "trapping light" were interchangeable while operating the system.

6.3.4 Cavity Probing and Light Detection

Actually coupling light into and measuring the light emitted from the cavity immediately bring in issues related to the quantum efficiency of a measurement. Consider, for example, that light is impinged on one side of the symmetric cavity with a detector placed on the other side. If the detector registers a "click," what has been learned about the state of the photon field inside the cavity? In practice the detector will register a certain photon count rate Γ_{meas}, and again the question is posed: what has been learned about the state of the photon field inside the cavity? All detectors will have "dark counts" which have nothing to do with the cavity at all. Furthermore, the cavity is twice as likely to scatter an intracavity photon as transmit it, and with a photodetector on only one side of the symmetric cavity the information gathered is reduced by another factor of two. Accounting for all of these effects is a budgeting of efficiencies and noise, and it is crucial to be very precise about these factors when making claims about measurements of a quantum system.

There are three main factors determining the efficiency of the measurements made herein. First, the cavity efficiency η_{cav} for the two-sided cavity (with one-sided detection) is given by $\eta_{cav} = \mathcal{T}/(2\mathcal{T} + 2\mathcal{L}) = 0.15$. Second, there will be losses on the optical path to the detector, and in this case the dichroic (CVI Laser LWP-45-RU720-TU850-PW-1008-C) and 780 nm interference filter (Intor 780/10/58-2R) which distill the probe

light from the 850 nm cavity locking light and background light contribute $\eta_{filt} = 0.74$. Finally, there is the efficiency of the detector itself. The Perkin-Elmer SPCM-AQR-13 single-photon counting module (SPCM) has a measured quantum efficiency at 780 nm of $\eta_{det} = 0.45$. These efficiencies are of course multiplicative, so the *maximum* total efficiency is $\eta = \eta_{cav}\,\eta_{filt}\,\eta_{det} = 0.05$.

We must also recognize the role played by background counts. The "dark counts" on the detector are an ever-present signal, and represent the absolute noise floor for any quantum optical measurement. The quoted dark count for the SPCM is 250 /s, but on the optical table [9] the measured dark count was $\Gamma_{d.c.} = 250 - 500$ /s. A second contribution to the background counts is the leakage of the 850 nm locking light. The dichroic mirror and interference filter prevent the typically ~ 100 nW of locking light emitted from the cavity from reaching the SPCM, which itself has a quoted detector efficiency at 850 nm of $\eta'_{det} \approx 0.45$. The SPCM background counting rate from the locking light leakage was typically $\Gamma_{850} = \eta'_{det}\Gamma_{leak} = 2 \times 10^4$ /s; in later implementations not treated in this thesis, these 850 nm leakage counts were eliminated below the dark count rate by use of a second dichroic mirror.

Thus, we have the full budget for the measured count rate Γ_{meas} with the equation

$$\Gamma_{meas} = (\eta_{det}\,\eta_{filt}\,\eta_{cav}) \times (2\kappa\bar{n}) + \Gamma_{850} + \Gamma_{d.c.}\,. \tag{6.19}$$

The conversion of measured count rate Γ_{meas} to the average intracavity photon number is thus

$$\bar{n} = 2.41\left(\frac{\Gamma_{meas}}{MHz}\right) - 0.05\,. \tag{6.20}$$

A graphical representation of the detection parameters is represented in Figure 6.8.

6.3.5 Atom Delivery to the Cavity

In terms of slowing, cooling, and delivering atoms to the millitrap region, the principles of operation are ultimately the same as described in previous chapters. While the system was designed to employ an Ioffe-Pritchard trap for ultracold atoms inside the cavity, we found we were unable to efficiently load atoms from the external quadrupole trap into IP

[9] With the rubber cap provided with the unit in place, the quoted dark count was approximately the specified 250 /s.

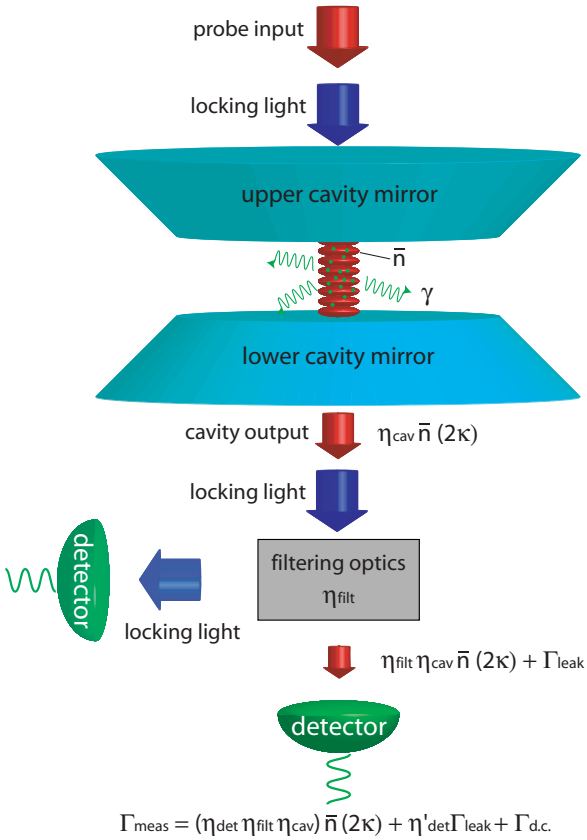

Figure 6.8: Many-atom cavity QED in the practice. N atoms are distributed over the cavity mode while 850 nm locking and 780 nm probe light are impinged on the cavity. (Note that there are in fact ~ 500 anti-nodes, and not the handful shown here for clarity.) The probe light establishes an average photon number of $\bar{n}$ inside the cavity, which decay at a rate 2κ from the cavity. The probability that this decay correlates to a photon emission toward the detector is η_c, and after factoring in the losses due to the filtering optics, the quantum efficiency of the detector,and the 850 nm leakage, we obtain a conversion formula (Equation (6.19)) for measured count rate to $\bar{n}$, the photonic state of the cavity.

trap in the presence of the cavity. The difficulty came about because the IP trap had to be biased with a transverse field to hold atoms the atoms outside the cavity, and as described in Ref. [54] this lowers the trap IP trap depth substantially for large deviations from the trap center. While we were able to load atoms into this shallowed trap, the transfer efficiency was so compromised that achieving runaway evaporative cooling became impossible.

As outlined in Section 3.5.3, 40,000 atom BECs were produced in a TOP trap 1 mm from the trap center. At $T \lesssim 1\,\mu$K, the atoms can be easily transported into the cavity

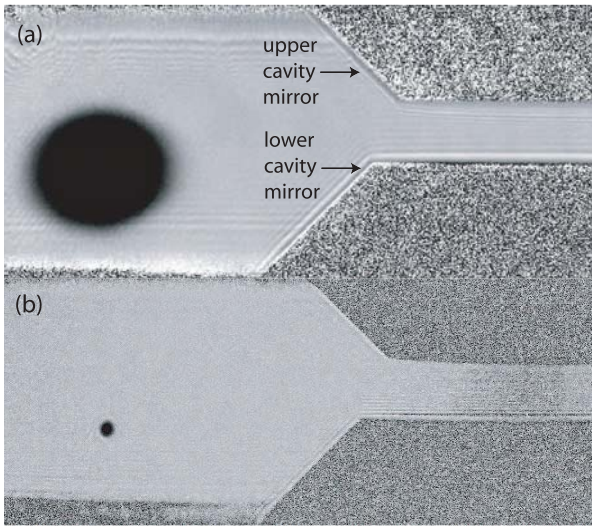

Figure 6.9: BEC in the TOP trap. (a) Atoms in the TOP trap before RF evaporation. Seen on the right are the shadows of the cavity mirrors. (b) After RF evaporation, a nearly pure condensate of 4×10^4 atoms is seen under 11 ms time of flight.

separation by displacing the position of the TOP center with bias field. One outstanding question prior to the delivery of cold atoms to the cavity was the lifetime of trapped atoms between the mirrors. While we certainly hoped it would be the same as the vacuum-limited lifetime outside the cavity, the outgassing properties of dielectric-coated mirrors was a large unknown and it didn't seem beyond the realm of possibility that the atoms would experience greater losses inside the narrow cavity due to increased background collisions. We directly compared the "inside" and "outside" lifetimes by holding a 1μK cloud in and out of the cavity, and measuring the atom decay from identical traps. Thankfully, we found that the lifetime inside the cavity (in the absence of probe light) slightly *surpassed* that outside the cavity region, though the improvement was not very significant.

6.4 Data Processing and Real-Time Detection

The output of the SPCM is an experimentalist's dream, a 5 V TTL pulse of width 30 ns. The dead time is ~ 70 ns, meaning only fluxes of $< 10^7$/s were allowed on a single SPCM. From Equation (6.20), this limits the intracavity photon number for the 780 nm

probe light to $\bar{n} \approx 20$.

We typically examined the SPCM data stream in two ways. For detailed processing, data was collected with a GageScope® digital oscilloscope which was operated with a dedicated[10] computer to collect the data. The duration of the data stream depended on the sampling rate of the oscilloscope, but it was typically operated at a sampling rate of 10 mega-samples-per-second (MSPS), which gave a 256 ms time window. For sensitive detection we would employ 50 MSPS, but there was little point in going any higher because the SPCM saturation count rate was 10 mega-counts-per-second (Mc/s). The data were stored in a dated file which required ~ 5 MB of disk space. Over the year and half of cavity operation, many data analysis routines (using Igor® software) have been developed to churn through these files to extract the information from the data stream. The workhorse was Deep Gupta's conversion program which converted the huge 5 MB analog Gagescope® files to a more manageable digital signal. These allowed very detailed analyses of the stream, though not yet in real time. This "post-processing" of the digital TTL output is non-ideal for experiments which need to discern the state of the system upon probing to trigger some other element, but is wonderful for hitting the "go" button for repeated experiments, going to Strada for a coffee, and returning to a set of data which the data analysis routines can batch through.

While it seems a perverse irony to take this beautiful (and pricey!) single photon counter and derive an analog signal from it, this is exactly the functionality that is needed to make the output of the device experimentally useful. Luckily, one gets to "have his cake and eat it too," as the signal from the SPCM may be split into two channels with only slight distortion of the $5\,V$, 30 ns square pulses[11] which are designed to be 50 Ohm-terminated. The first split channel inputs to the GageScope® (with an inline 50 Ohm terminator), the second to a device constructed to convert the count rate to an analog voltage (with a high-impedance input). Commercial count-rate-to-voltage converters (CRVCs) are available, but are typically designed for high count rates. To convert the cavity signal (which can

[10] This computer's processor was also heavily dedicated towards daily music consumption (KLM), cricket scores (Deep), and scouring Craigslist for $1,000 cello bows (Kater).

[11] The distortion typically took the form of a "ringing," where the pulse was presumably reflected on the BNC cable line and resulted in ~ 3 pulses of decaying amplitude. Both the GageScope® and the CRVC could be tuned to disregard these after-events.

be as low as 1000 counts/sec) to an analog voltage which is tailored to the SPCM output, we designed a CRVC circuit with a tunable bandwidth from $1 - 250$kHz with just $2\,\mu$s of dead time per cycle. Figure 6.10 describes the timing diagram, and Figure 6.11 shows the details of the electronic elements.

The CRVC thus allows the use of the SPCM as both a highly sensitive photodiode and a digital photon counter. The analog output of the CRVC is input to an Agilent digital oscilliscope, allowing sensitive triggering of the cavity flux to within the inverse of the CRVC bandwidth. With this element, we obtain a real-time monitor of the cavity transmission, and thereby the state of the atoms in the cavity mode. As described in the following chapter, many experiments relied on this functionality to initialize the system.

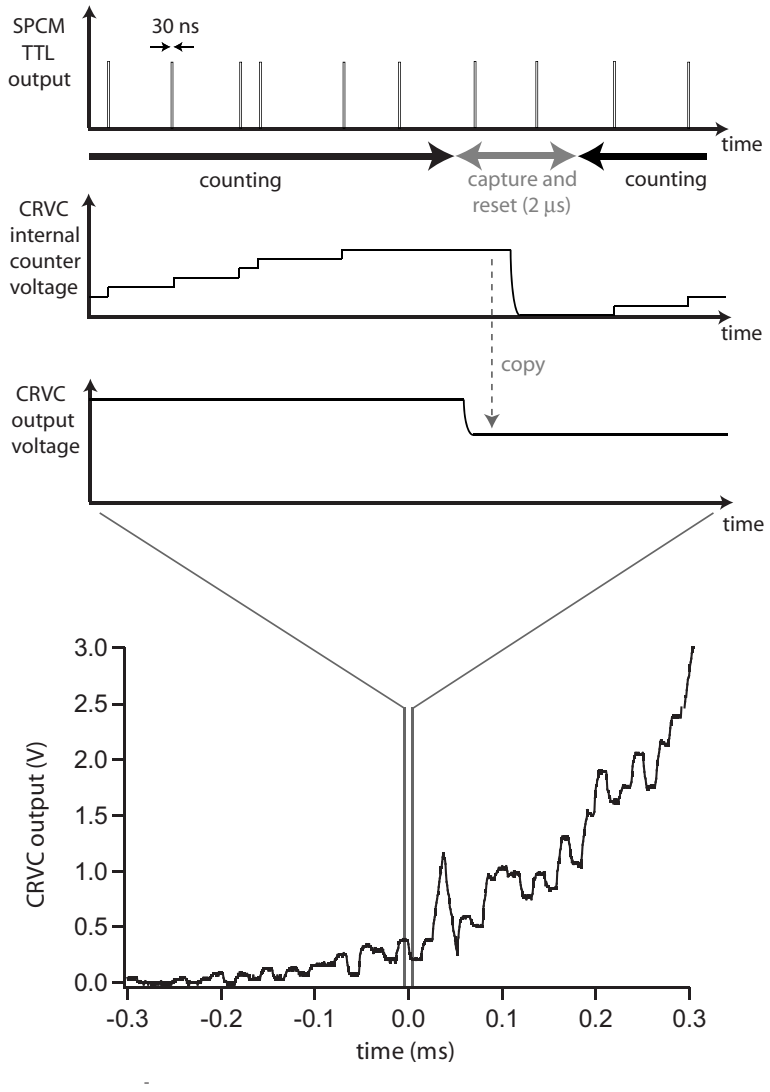

Figure 6.10: The count-rate-to-voltage converter (CRVC) timing diagram. The upper trace shows the SPCM output as 30 ns TTL pulses, which are input to the CRVC circuit which increments the counter during the "capture" time. The clock cycle has 2 μs dead time, during which the count number is "copied" to the output value of the CRVC, the counter is subsequently cleared, and finally the count for the next clock cycle begins from zero. The bottom trace shows what the output of the CRVC looks like as the cavity comes into resonance in the presence of a probe, and many experiments described in the following chapter are initialized by this rising edge harkening the arrival of the cavity resonance condition.

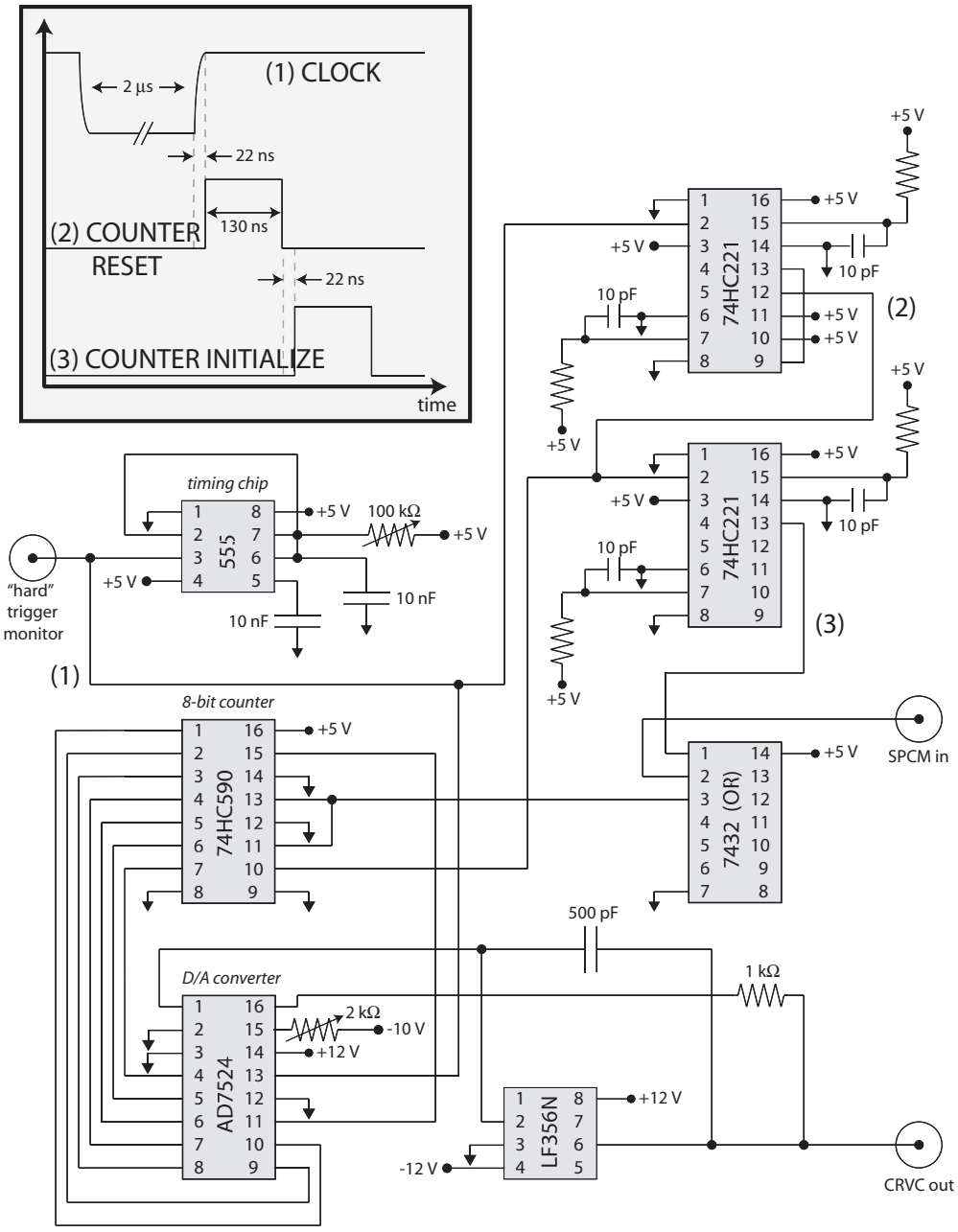

Figure 6.11: Count-rate-to-voltage converter circuit diagram.